Comparing Matched Polymer:Fullerene Solar Cells Made by Solution-Sequential Processing and Traditional Blend Casting: Nanoscale Structure and Device Performance

Steven A. Hawks,[†] Jordan C. Aguirre,[‡] Laura T. Schelhas,[‡] Robert J. Thompson,[‡] Rachel C. Huber,[‡] Amy S. Ferreira,[‡] Guangye Zhang,[‡] Andrew A. Herzing,[∥] Sarah H. Tolbert,*[,†,‡,§] and Benjamin J. Schwartz*[,‡,§]

[†]Department of Materials Science and Engineering and [‡]Department of Chemistry and Biochemistry, University of California, Los Angeles, Los Angeles, California 90095-1569, United States

[§]California NanoSystems Institute, University of California, Los Angeles, Los Angeles, California 90095, United States

[∥]Materials Measurement Science Division, Material Measurement Laboratory, National Institute of Standards and Technology, Gaithersburg, Maryland 20899, United States

S *Supporting Information*

ABSTRACT: Polymer:fullerene bulk heterojunction (BHJ) solar cell active layers can be created by traditional blend casting (BC), where the components are mixed together in solution before deposition, or by sequential processing (SqP), where the pure polymer and fullerene materials are cast sequentially from different solutions. Presently, however, the relative merits of SqP as compared to BC are not fully understood because there has yet to be an equivalent (composition- and thickness-matched layer) comparison between the two processing techniques. The main reason why matched SqP and BC devices have not been compared is because the composition of SqP active layers has not been accurately known. In this paper, we present a novel technique for accurately measuring the polymer:fullerene film composition in SqP active layers, which allows us to make the first comparisons between rigorously composition- and thickness-matched BHJ organic solar cells made by SqP and traditional BC. We discover that, in optimal photovoltaic devices, SqP active layers have a very similar composition as their optimized BC counterparts (≈44−50 mass % PCBM). We then present a thorough investigation of the morphological and device properties of thickness- and composition-matched P3HT:PCBM SqP and BC active layers in order to better understand the advantages and drawbacks of both processing approaches. For our matched devices, we find that small-area SqP cells perform better than BC cells due to both superior film quality and enhanced optical absorption from more crystalline P3HT. The enhanced film quality of SqP active layers also results in higher performance and significantly better reproducibility in larger-area devices, indicating that SqP is more amenable to scaling than the traditional BC approach. X-ray diffraction, UV−vis absorption, and energy-filtered transmission electron tomography collectively show that annealed SqP active layers have a finer-scale blend morphology and more crystalline polymer and fullerene domains when compared to equivalently processed BC active layers. Charge extraction by linearly increasing voltage (CELIV) measurements, combined with X-ray photoelectron spectroscopy, also show that the top (nonsubstrate) interface for SqP films is slightly richer in PCBM compared to matched BC active layers. Despite these clear differences in bulk and vertical morphology, transient photovoltage, transient photocurrent, and subgap external quantum efficiency measurements all indicate that the interfacial electronic processes occurring at P3HT:PCBM heterojunctions are essentially identical in matched-annealed SqP and BC active layers, suggesting that device physics are surprisingly robust with respect to the details of the BHJ morphology.
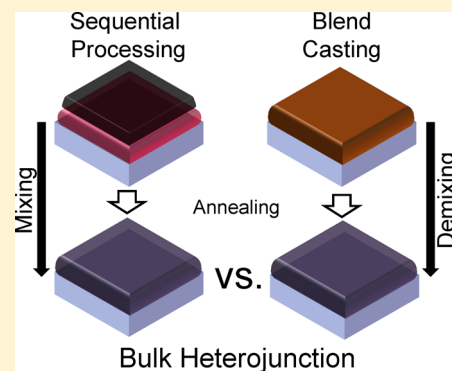
1. INTRODUCTION

Photovoltaics based on mixtures of semiconducting polymers and functionalized fullerenes have attracted significant interest as low-cost solar energy harvesters.[1] Improvements in device architecture and polymer design have yielded single-junction power conversion efficiencies (PCEs) above 9%[2] and tandem-cell efficiencies over 10%.[3−5] The ability to achieve high PCEs with these materials is predicated on forming a nanoscale

polymer−fullerene network, known as a bulk heterojunction (BHJ), that must simultaneously dissociate excitons, transport separated mobile charges, and suppress recombination of excess photogenerated carriers.[6,7] An extensively studied approach for

creating such networks is the blend-casting (BC) method, wherein the polymer and fullerene are dissolved together in solution and then cast into a thin film. This approach is highly sensitive to processing conditions and to material properties because it relies on poorly understood spontaneous nanoscale phase separation to create the desired donor–acceptor network morphology.[8] Thus, even though the BC approach is simple and amenable to extensive optimization, it introduces irreversible interdependencies between material properties, processing, and morphology that limit control over BHJ network formation and thus also device performance.[9,10] Additionally, with the BC approach, it is difficult to determine if an optimized morphology is kinetically trapped and unstable or near a reasonable thermodynamic minimum and thus is more suitable for long-term solar energy harvesting.

Recently, we presented an alternative to the BC method that involves sequential deposition of the polymer and fullerene layers from semiorthogonal solvents.[11,12] This solution sequential-processing (SqP) route involves interdiffusing the acceptor molecule into a precast donor underlayer. Although it involves two processing steps for the active layer instead of one, the SqP method is advantageous for making a BHJ compared to the BC method because it affords more control over the polymer:fullerene network formation while still preserving device efficiency and the ease of solution-based fabrication.[13–18] A schematic illustrating the methodology behind these two processing routes is presented in Figure 1. Though initially
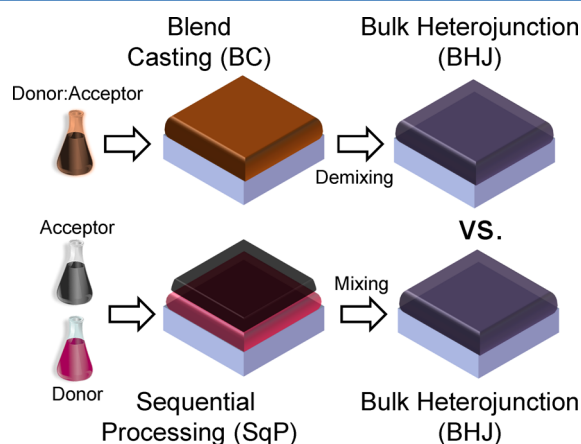

Figure 1. Active-layer BHJ formation approaches for the SqP and traditional BC methods. The SqP method creates a BHJ network by interdiffusion of the acceptor into a host donor matrix, whereas the traditional BC approach relies upon spontaneous nanoscale phase separation. The questions we aim to address here are: is the final BHJ structure from the two methods the same, or not, and what implications does the respective processing route have for device performance?

misunderstood,[11] it is now accepted that extensive mixing of the donor and acceptor components must occur for optimal SqP device performance.[17–25] These interdiffusion processes in SqP result from selective swelling of the amorphous regions of the (donor) underlayer with the solvent used to deposit the (acceptor) overlayer material. Additionally, thermal diffusion from annealing can be used to intermix the two components. The added versatility of this interdiffusion-based SqP approach has allowed researchers to better understand the underlying factors that give rise to functional polymer:fullerene morphologies and to use techniques that are inapplicable or detrimental

to the BC method.[26–37] For instance, the polymer layers in the SqP approach are amenable to cross-linking,[33,34] chemical doping,[26] nanopatterning,[36,38,39] polarization by chain alignment,[37] and controlled solution-based deposition using a gas-permeable cover layer,[35] whereas these treatments are typically harmful or nonbeneficial to BC device performance.[40] Recently, the SqP approach also has surpassed the BC method in comparisons of globally optimized device performance in multiple semiconducting polymer systems.[41,42]

Despite all of these advantages, there still has not been a stringent comparison of the nanoscale networks formed via SqP and BC to determine what differences, if any, exist between them. The main reason for this lack of comparison is that the polymer:fullerene film composition in the SqP processing route is not accurately known because the components are deposited separately instead of from a premixed solution. To the best of our knowledge, only approximate, indirect estimates of the SqP film composition have been made using a variety of methods, including solid-film UV–vis absorption spectroscopy,[43] photoluminescence (PL) quenching,[18] neutron reflectivity,[17,19] and time-resolved microwave conductivity (TRMC).[20] Since all of this previous work gives only approximate compositions, the overall morphology/processing/performance relationships are not well-known for SqP active layers, so equivalent head-to-head comparisons of the two approaches summarized in Figure 1 have not been carried out to date.

In this article, we present a rigorous comparison of the nanoscale morphological and photovoltaic properties of composition- and thickness-matched SqP and BC bulk heterojunction solar cells made from active layers composed of poly(3-hexylthiophene-2,5-diyl) (P3HT) and [6,6]-phenyl C_{61} butyric acid methyl ester (PCBM). To do this, we first developed a new method for accurately determining the overall SqP film composition and then used this method to produce composition- and thickness-matched BC and SqP layers. When examining these thickness- and composition-matched BC and SqP P3HT:PCBM solar cells, we find that the optimal SqP active-layer composition is between 44 and 50 mass % PCBM. This is more PCBM-rich than expected based on our previous work[20,43] and lies in the same optimal regime as BC P3HT:PCBM films.[44] Furthermore, structural characterization shows that SqP films have a higher degree of both polymer and fullerene molecular ordering than equivalent BC films and that the SqP P3HT:PCBM films are blended on a slightly finer scale than the matched BHJs produced by BC. Despite these differences in molecular crystallinity and nanoscale BHJ morphology, matched SqP and BC films have remarkably similar electronic and photovoltaic properties in small-scale devices. However, when we compare matched films in larger active area devices, the SqP route yields higher device performance and significantly better reproducibility due to enhanced film quality. Overall, even when matched as closely as possible, SqP and BC produce different nanoscale BHJ architectures; however, these different architectures lead to similar device performance (in small active areas), showing that polymer-based BHJ photovoltaics surprisingly can tolerate a fair range of nanometer-scale BHJ structures.

2. METHOD FOR DETERMINING THE COMPOSITION OF POLYMER:FULLERENE FILMS

Experimental details for the standard, well-established, techniques used in this work can be found in the Supporting
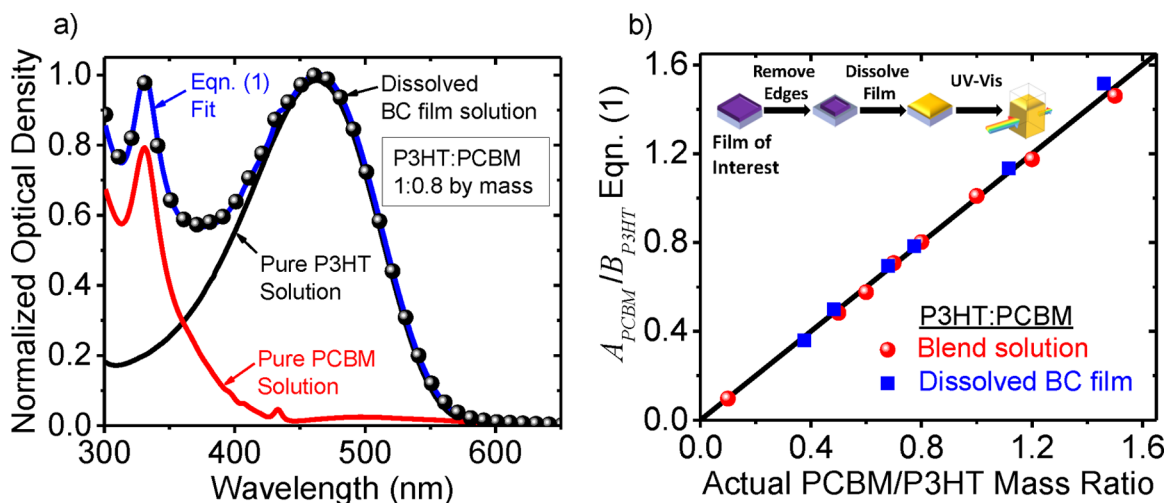
Figure 2. (a) Solution-phase absorption spectrum (blue curve) of a redissolved 1:0.8 P3HT:PCBM weight ratio BC film (obtained from the procedure shown in the inset of panel b), along with its fit to a linear combination of the pure solution-phase P3HT (black curve) and PCBM (red curve) components. (b) Test of this procedure on BC films and solutions with known composition. The fitted P3HT:PCBM mass ratio (eq 1) of BC solutions (red spheres) and redissolved BC films (blue squares) as a function of their actual mass ratio; the black line is a reference with slope 1 and intercept zero. Clearly, the solution UV–vis of a redissolved blend film can accurately recover the film's composition. Each point is the average of three substrates/solutions, and the error bars (one standard deviation) are smaller than the plotted symbols.

Information. Here we detail only our original method for obtaining the composition of SqP active layers.

SqP films were made by casting a PCBM overlayer dissolved in dichloromethane (DCM) on top of a predeposited 130 ± 5 nm thick P3HT underlayer cast from o-dichlorobenzene (ODCB). Since the amount of PCBM deposited onto the P3HT film is unknown, the total mass ratio of P3HT to PCBM in the final film is also not known. Although it may seem safe to assume that UV–vis absorption measurements on thin-film samples can be used to calculate solid-state film compositions, in fact the polymer extinction coefficients can vary significantly with the crystallinity of the polymer, and a myriad of other effects also can affect solid-film absorbance measurements (e.g., scattering, interference, reflectivity, etc.). As a result, the composition cannot be accurately determined from solid-state optical absorption, as will be revealed in detail below.

Instead of using solid-film absorbance measurements, our approach for determining an active layer's stoichiometry involves redissolving the film after casting/processing and fitting the resulting dilute-solution absorption spectrum to a linear combination of the individual-component spectra (Figure 2a and inset to Figure 2b). Procedurally, we first remove the outer edges of the film with a razor, leaving only the area where solar cells are fabricated. We scratch away the outer edge of the films as a precautionary measure because by eye this region looks different, and it has no relevance to the questions at hand. Once the edges are removed, the active layer is then redissolved in ODCB and transferred to a 1 mm thick cuvette. Even after thermal annealing, we found that P3HT:PCBM films readily dissolve in ODCB. We carried out the redissolving/washing step at least 3−4 times for each film in order to fully remove all material from the surface of the substrate. If the substrate was insufficiently cleaned, the compositions determined for BC films appeared anomalously rich in PCBM by roughly 10 mass %. We suspect that these anomalous compositions arise from insufficient cleaning are due to the higher propensity for P3HT to remain on the substrate rather than enter solution upon redissolving. Fortunately, this issue can be easily avoided by simply washing away the entirety of the film. The final solutions

typically had peak optical densities in the range of 0.1−0.2 and concentrations on the order of 0.05 mg/mL for each component.

Figure 2a shows the solution-phase absorption spectrum of a redissolved 1:0.8 P3HT:PBCM mass ratio BC film (black circles) along with a fit (blue curve) of the absorption to the sum of the individual solution-phase components:

$$\mathrm{OD}_{\mathrm{Soln}}(\lambda) = A_{\mathrm{PCBM}}\mathrm{OD}_{\mathrm{PCBM}}(\lambda) + B_{\mathrm{P3HT}}\mathrm{OD}_{\mathrm{P3HT}}(\lambda) \quad (1)$$

where A_{PCBM} and B_{P3HT} are fitting coefficients representing the amount of each material, $\mathrm{OD}_{\mathrm{Soln}}(\lambda)$ is the measured optical density of the composite (dissolved film) solution, $\mathrm{OD}_{\mathrm{PCBM}}(\lambda)$ is the normalized optical density of a dilute pure PCBM solution in ODCB (red curve), and $\mathrm{OD}_{\mathrm{P3HT}}(\lambda)$ is the normalized optical density of a dilute pure P3HT solution in ODCB (black curve). We fit the entire solution spectrum to take advantage of the full spectral information and also to minimize/recognize any effects of impurities or aggregation. We found that the fits to eq 1 were excellent (Figure 2a is typical) and unaffected by the use of different P3HT or PCBM material batches or extensive thermal annealing. Clearly this approach is general and can be extended to a wide range of soluble organic molecule combinations.

Since the dilute redissolved solutions faithfully follow Beer's law with invariant extinction coefficients, the ratio of the fitted coefficients $A_{\mathrm{PCBM}}/B_{\mathrm{P3HT}}$ is equal to the PCBM/P3HT mass ratio of the solution/redissolved film. To confirm this, Figure 2b plots the ratio of eq 1 fit coefficients for as-prepared dilute BC solutions (red circles) as a function of their actual PCBM/P3HT mass ratio. As expected, all points fall on a line of slope one and intercept zero. Figure 2b also plots the ratio of eq 1 fit coefficients obtained from a series of redissolved BC films (blue squares) as a function of their actual mass ratio, which falls on the same line of slope one and intercept zero, proving that a film's composition can be accurately determined by our method. We note that the dissolved BC film data in Figure 2 are averages over three separate substrates with standard deviations that are smaller than the symbol size, demonstrating that the method is highly reproducible.

3. COMPARING THE ACTIVE-LAYER COMPOSITION AND MORPHOLOGY OF MATCHED SqP AND BC P3HT:PCBM FILMS

3.1. Revealing the SqP Film Composition. After establishing that our composition measurement technique was accurate and reproducible, we applied it to P3HT:PCBM SqP films processed over a range of conditions representative of what is employed in the literature.[11,23,24,31] Figure 3 shows SqP
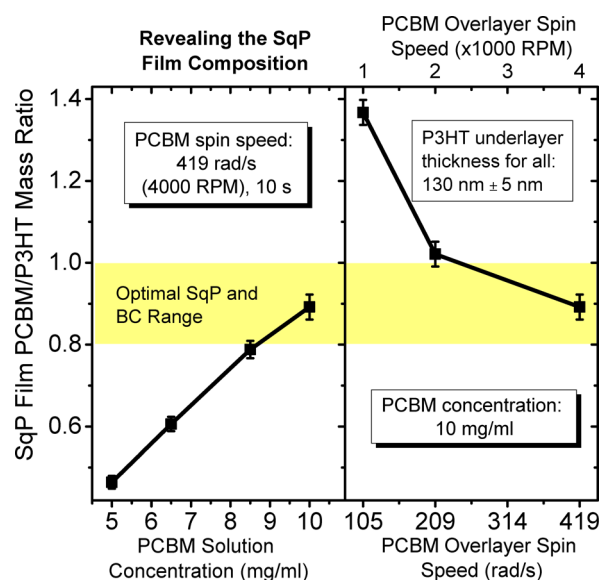

Figure 3. Composition of P3HT/PCBM SqP active layers as a function of the PCBM solution concentration in DCM and spin speed used to create the overlayer. In all cases the P3HT underlayer was 130 ± 5 nm thick. In this comparison, the optimal conditions for SqP solar cell performance (cf. Figure 7) are 10 mg/mL, 419 rad/s (4000 rpm), and 10 s. The optimal BC solar cell composition range is from ref 44.

film compositions resulting from a series of active layers made by casting a PCBM overlayer from DCM with a variety of different concentrations and spin speeds on top of a predeposited 130 ± 5 nm thick P3HT underlayer (see Supporting Information for more detailed experimental procedures). The results in Figure 3 show that SqP films are richer in PCBM than would be expected based upon our previous estimates.[20,43] When we fabricated photovoltaic devices out of these active layers, we found that the optimal device performance was achieved when the overlayer was spun from a 10 mg/mL PCBM solution in DCM at a spin speed of 419 rad/s (4000 rpm), which corresponded to film compositions with mass ratios between 1:0.8 and 1:1 P3HT:PCBM. We found that the run-to-run compositions we obtained were highly reproducible when using solutions of PCBM in DCM with concentrations less than 8 mg/mL but that the commonly used 10 mg/mL concentration was too near the PCBM solubility limit and gave run-to-run results that varied between 1:0.8 and 1:1 P3HT:PCBM by mass for the same spin conditions. In a particular run, though, we found that a 10 mg/mL PCBM solution in DCM can give reproducible compositions (Figure 3 error bars). In comparing the results of Figure 3 to previously reported processing conditions for P3HT:PCBM SqP devices, we conclude that optimal P3HT:PCBM SqP active layers have a composition in the same range as their optimal BC counterparts (1:0.8 to 1:1 P3HT:PCBM mass ratio; yellow bar in Figure 3), which is

surprising because it is not necessarily obvious that SqP should have the same optimal composition as BC.[11,44−48] Additionally, in the Supporting Information (Figure S4) we show that a PCBM content of ≈1:0.8 in SqP devices is necessary for good device performance, and that SqP active layers do not operate well at lower PCBM contents.

Figure 3 further shows that the SqP film composition can be tuned over a wide range from 31 mass % PCBM (1:0.45 weight ratio) to 58% PCBM by mass (1:1.37 weight ratio) by simply changing the processing parameters for the PCBM overlayer (i.e., solution concentration and spin speed). This allows us to make better sense of the wide range of processing conditions in the literature for P3HT:PCBM SqP films.[18−21,23,24,26,45,46] Figure 3 suggests that when optimizing an SqP active layer for device performance, the PCBM solution concentration and deposition conditions are tuned for a given P3HT underlayer to achieve a composition that is approximately the same as the optimal composition for an equivalent BC film. Finally, we also note that compositions for processing-condition combinations not indicated in Figure 3 can be estimated from linear extrapolation from the data in Figure 3. This analysis also can be extended to previously published SqP morphology studies where the overall composition was unknown.[17,19,46]

3.2. Morphology Differences of Matched SqP and BC P3HT:PCBM Films. Given that the optimal device processing conditions lead to SqP active layers with a similar composition as that for optimal BC films, the next important question we ask is whether or not the two different processing routes produce the same nanoscale BHJ architecture. There have been claims that SqP simply provides a more complex route to the same BHJ structure as BC,[45,46] so it is important to determine if thickness- and composition-matched films produced via SqP and BC have the same morphology. To investigate this question, we fabricated a series of 1:0.8 P3HT:PCBM mass ratio active layers via SqP, determining the composition as above, and then made corresponding BC films with matching composition and thickness (see Supporting Information for the detailed matching recipe). In the following analysis, when we refer to "matched" BC and SqP films, we mean films with identical 1:0.8 composition ratios and identical total thicknesses of 165 nm.

We begin by examining absorption spectra of matched films produced by the two different processing routes since the absorptive features of P3HT directly reflect its molecular ordering.[49] Figure 4 shows the thin-film absorbance of matched annealed P3HT:PCBM SqP and BC films prepared in the manner described in the Supporting Information. When compared to the equivalent BC film, the P3HT:PCBM SqP film shows stronger absorbance in the region associated with aggregated P3HT as well as more pronounced vibronic structure.[49] We note that when repeating this measurement, the absorbance of SqP films was more reproducible than the corresponding BC films because the absorption of BC films is highly sensitive to drying history, irrespective of thermal annealing (see Supporting Information Figure S1).[50] Although this sensitivity to drying is especially prevalent with P3HT-based BC films, aggregation-dependent absorption is a feature of many molecular materials that are of interest for SqP solar cells.[51] Thus, Figure 4 provides the first evidence that SqP films are less sensitive to processing kinetics than BC films, showing that SqP can yield high-quality active layers that are less affected by the details of the drying conditions.
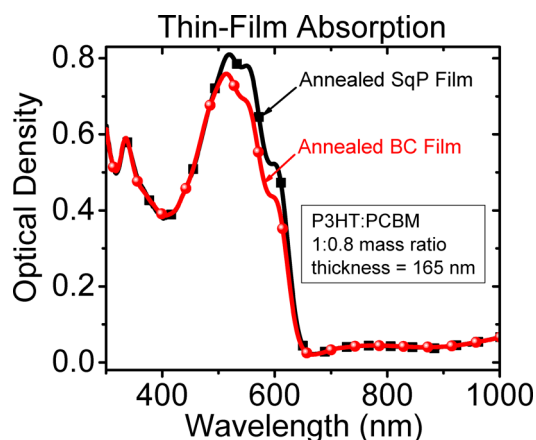
Figure 4. Solid-film absorbance 1:0.8 P3HT:PCBM weight ratio, 165 nm thick matched SqP and BC films that were thermally annealed for 20 m at 150 °C. The significant difference in absorbance is due to differences in P3HT crystallinity. The well-matched features in the near-IR region, due to thin-film interference, show that the two films indeed have similar thickness.

Figure 5. GIXD data of matched 1:0.8 P3HT:PCBM SqP and BC films after thermal annealing for 20 m at 150 °C, showing stronger diffraction in the SqP active layer. Each curve represents the integrated intensity at each q averaged over three separate films.

Perhaps more importantly, as discussed above, Figure 4 also demonstrates that solid-film UV–vis absorbance cannot be used to obtain reliable composition estimates: the two films whose spectra are shown in Figure 4 have identical compositions and thickness but different absorbances. This is because the polymer absorption spectrum depends sensitively on its local environment (e.g., degree of (para)crystallinity, orientation, crystallite size, etc.). Additionally, solid-film absorption measurements are strongly affected by reflectivity, scattering, and thin-film interference,[52] so that there is no simple way to extract the composition. Thus, it is critical that our redissolving method be used if accurate and reproducible composition estimates are desired.

The differences in the spectra in Figure 4 also suggest that, in the present comparison, the P3HT in the SqP films is more crystalline than in matched, equivalently processed BC films. The reason for this is that with SqP there is no PCBM to inhibit aggregation when the polymer film is cast. This is an important difference to consider when attempting to tailor a polymer underlayer for ideal network formation. The effects of annealing and interdiffusion on the SqP absorbance are presented in the Supporting Information (Figure S3), showing that the P3HT absorbance for SqP films is unchanged by incorporation of the PCBM. We note, however, that slow-drying of BC films can result in a similar polymer film absorbance and thus presumably similar levels of P3HT aggregation. For this work, however, we did not slow dry the BC films because we wanted to make the best head-to-head comparison with the SqP approach, which involves thermal annealing instead of slow drying. We also note that our chosen postprocessing conditions for BC P3HT:PCBM devices yield similar solar cell performance to devices made by slow drying.[53]

Although absorption spectroscopy can provide a general indication as to the relative crystallinity of P3HT in different film environments, it does not provide detailed information about the morphology of the polymer:fullerene networks in such films. Thus, we examined the structure of our matched annealed SqP and BC films using grazing-incidence X-ray diffraction (GIXD). Although we collected the diffraction in 2-D (Supporting Information Figure S7), Figure 5 shows the radially integrated data, which immediately provides a sense of
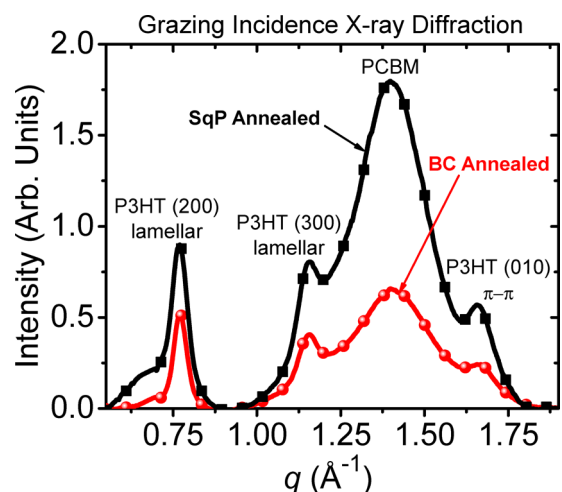
the relative degree of crystallinity of the components in each of the matched films. We emphasize that this integrated data is representative of the differences in molecular order between SqP and BC films because the experiment was conducted on multiple samples that were rigorously thickness- and composition-matched and examined under identical beamline conditions (see Supporting Information for experimental and analysis details). Indeed, Figure 5 confirms the general conclusion we drew from Figure 4, showing not only that the P3HT but also the PCBM exhibits stronger diffraction in annealed SqP active layers. In particular, Figure 5 shows that both the P3HT lamellar and $\pi-\pi$ stacking order is greater in SqP films. Further analysis of the P3HT (100) (not shown) and (200) peaks, however, reveals that the full width half-maximum (fwhm) of the diffraction peaks is slightly larger for SqP derived layers (fwhm$_{(100)}$ = 0.039 Å^{-1} and fwhm$_{(200)}$ = 0.073 Å^{-1}) than BC films (fwhm$_{(100)}$ = 0.035 Å^{-1} and fwhm$_{(200)}$ = 0.053 Å^{-1}), suggesting that despite increased order (which would likely decrease the fwhm), the SqP morphology appears to produce smaller domain sizes, a conclusion we support with energy-filtered TEM tomography below. The stronger PCBM diffraction in SqP films observed in Figure 5 also could be partly due to the presence of a pure, thin PCBM overlayer on top of the annealed SqP film, which would be consistent with the XPS results presented below.

As briefly mentioned above, there are good reasons why P3HT:PCBM SqP active layers should have more ordered domains when compared to equivalent BC active layers. BC films rely on spontaneous nanoscale phase separation during film formation, which means that P3HT crystallization occurs in the presence of a significant amount of PCBM. This initial presence of PCBM will therefore play a significant role in determining the final P3HT morphology as the blend transitions from solution to solid film. With SqP P3HT:PCBM active layers, on the other hand, the neat P3HT underlayer is already formed and in the solid state when the PCBM is introduced. During interdiffusion into the polymer matrix, the PCBM primarily intercalates into the amorphous regions of the P3HT,[11] allowing the high initial crystallinity to remain intact throughout processing (Figure S3).[26,25] Thus, PCBM has a
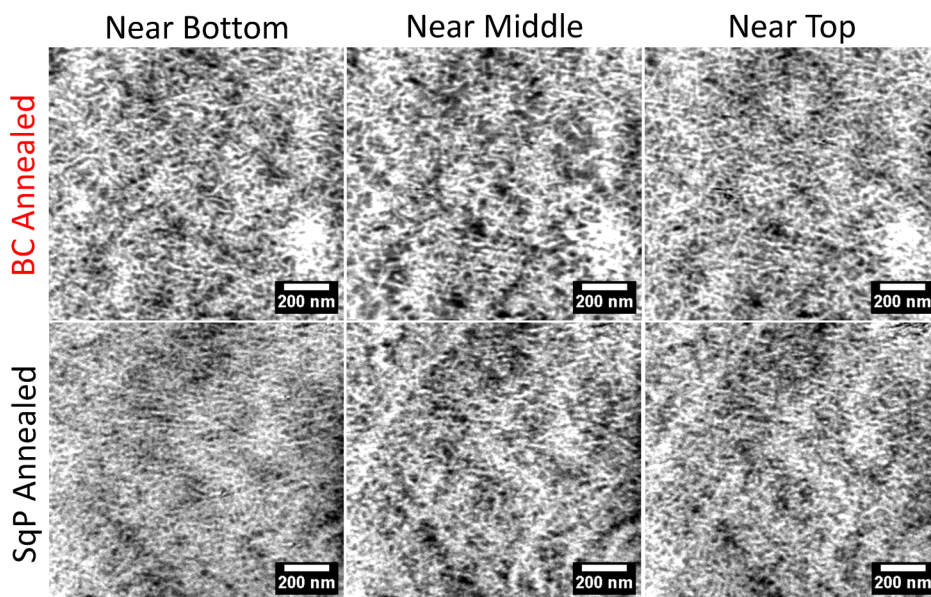
Figure 6. EF-TEM tomography slices of matched-annealed SqP and BC films showing the $x-y$ plane (parallel to the substrate plane) for near the top (film/air interface), middle, and bottom (film/substrate interface) regions of the films (see Supporting Information for details on how the contrast was obtained). The SqP film has an overall finer nanometer-scale structure, especially in the region near the substrate; see text for details.

significantly reduced role in determining the overall morphology in the SqP approach as opposed to the BC approach.

Lastly, we performed energy-filtered transmission electron microscopy (EF-TEM) and tomography to examine the morphologies of our matched-annealed SqP and BC films (Figure 6). In EF-TEM, images of the specimen are formed using electrons that have lost a specific amount of energy. This imaging mode can be combined with electron tomography techniques to produce a three-dimensional reconstruction of the specimen from a series of two-dimensional EF-TEM projections. This technique has proven quite useful for P3HT:PCBM devices, where the contrast produced in conventional bright-field TEM imaging is much lower due to the similar electron scattering characteristics of the two constituent materials. Several groups have reported results using EF-TEM tomography to image the nanoscale morphology of P3HT:PCBM devices.[54−57] Our images were collected in a similar fashion to this previous work (see Supporting Information for details regarding data acquisition and processing).

Figure 6 displays the results of this procedure for the thickness- and composition-matched annealed SqP and BC active layers. In-plane slices extracted from near the top (film/air), middle, and bottom (film/PEDOT) sections of the EF-TEM tomograms show the vertical distribution of the P3HT-rich domains (bright) and PCBM-rich domains (dark). The most striking differences in morphology exist near the substrate interface, where it is clear that the SqP film has a much finer nanometer-scale structure (Figure 6).[58] Moving vertically through the film toward the top surface (film/air) shows that the matched SqP and BC active layers converge to a more similar morphology, though the SqP has consistently smaller overall domains and a finer structure (as also observed by GIXD, above). We also note that EF-TEM is not surface sensitive, and thus the near-top images in Figure 6 are actually buried slightly below the top surfaces that are analyzed in the next section by XPS and CELIV.

We hypothesize that the fine structure of the SqP film morphology derives from the fact that polymer-layer formation occurs in the absence of PCBM. When PCBM is present in large amounts, as in the BC case, it carves out significant volume during film formation. Upon annealing and polymer/fullerene separation, some of the blended volume becomes available for the P3HT to use in forming larger domains. In SqP, the polymer matrix is already in the solid state, and thus interdiffusion of PCBM does not significantly alter its fine structure. Hence, in the BC case, the initial presence of PCBM plays a more significant role in determining the polymer morphology.

Although there are structural differences evident in Figure 6, given the significantly different processing routes used (Figure 1), it is somewhat surprising that the two BHJ networks are generally so similar. This suggests that for the P3HT:PCBM materials combination, formation of a BHJ network on this length scale can be achieved by multiple processing routes.[46] However, our comparison of matched films using GIXD and EF-TEM does show that the morphology obtained by the traditional BC approach has larger and less ordered material domains when compared to the SqP morphology, although both BHJs have structure on similar length scales.

3.3. Top-Surface Composition of Matched SqP and BC P3HT:PCBM Films. In addition to the overall crystallinity of the components of a BHJ, photovoltaic performance also can depend on the degree of vertical phase separation, i.e., the composition distribution of the components in the direction normal to the plane of the film.[59,60] Since SqP films (prior to thermal annealing) start with most of the fullerene on top, one might expect that the degree of vertical phase separation could be different in films produced via SqP and BC. To determine if there actually is any difference, we measured the top and bottom surface compositions of our matched annealed SqP and BHJ active layers using X-ray photoelectron spectroscopy (XPS).

For P3HT:PCBM blend films, XPS can provide an estimate of the average surface composition by measuring the sulfur-to-

17418

dx.doi.org/10.1021/jp504560r | *J. Phys. Chem. C* 2014, 118, 17413−17425

carbon (S/C) ratio since the PCBM component does not contain sulfur.[61−63] By fitting the sulfur 2p and the carbon 1s spectral lines (see Supporting Information for experimental and analysis details), we found that the top (film/air) surface of annealed SqP films is slightly richer in PCBM when compared to annealed BC films (see Table 2). A statistical *t*-test for the annealed top-surface data gives a significance level of $p = 0.106$, indicating with a reasonable degree of confidence that the surface composition is indeed slightly different, with the SqP film having marginally more fullerene on the top surface than the BC sample. The S/C ratio of as-cast SqP films, on the other hand, is smaller than the annealed layer's S/C ratio by more than an order of magnitude (Table 2). This confirms that the top surface of as-cast SqP P3HT/PCBM films are covered by PCBM with only a very small fraction of P3HT, in agreement with previously published XPS and neutron reflectivity experiments.[17,19] Interestingly, the bottom surface of both SqP and BC films are significantly enriched in fullerene (Table 2), but there is no statistically significant difference in S/C ratio for annealed films. Thus, our XPS results indicate that one difference between matched-annealed P3HT:PCBM SqP and BC films is that annealed SqP films are slightly richer in PCBM at the top surface, a remnant of the initial SqP as-cast quasi-bilayer structure.

As a way to better understand how differences in surface composition can affect device characteristics, we measured the equilibrium dark doping density of our matched BC and SqP films using the CELIV technique.[64] In CELIV, a linear reverse-bias voltage ramp is applied to a device and the resulting current is monitored. Most of the measured signal in this experiment results from displacement current, since the device acts as a capacitor, but if there are any mobile carriers present due to doping, CELIV can easily and accurately measure their presence. Integrating the CELIV transients (see Supporting Information Figure S5) after subtracting the displacement current gives the results that are summarized below in Table 2. We find that there is indeed a correlation between the average doping density measured by CELIV and the top-surface PCBM content determined by the XPS S/C ratio. Specifically, the as-cast SqP films have a substantial number of carriers in the dark at zero bias, whereas annealed SqP devices have ≈7 times less and annealed BC films have an undetectable ($\leq \sim 10^{14}$ cm^{-3}) number of dark carriers. To explain these results, we hypothesize that the Ca cathode is doping PCBM at or around the top interface (the device structure is ITO/PEDOT:PSS/ P3HT:PCBM/Ca/Al). This is consistent with other studies[65−67] and provides further verification that annealed SqP films have more PCBM on their top surface than equivalent BCs. Moreover, this shows that CELIV can be used as a simple and sensitive tool for examining the relative amount of fullerene material at the metal/active-layer contact. We note that hole doping of the P3HT from chemical contaminants cannot be responsible for the CELIV signals because all the materials were made using P3HT from the same batch and all the solutions underwent identical processing. In the next section, we explore how these morphological vertical composition differences affect the performance of photovoltaic devices.

4. COMPARING THE DEVICE PHYSICS OF MATCHED SqP AND BC P3HT:PCBM PHOTOVOLTAIC DEVICES

4.1. Solar Cell Performance of Matched BC and SqP P3HT:PCBM Films.
Now that we understand the similarities and differences in the nanometer scale morphology of

thickness- and composition-matched BC and SqP films, we turn to photovoltaic devices based on these films. The details of how the devices were fabricated are described in the Supporting Information. Figure 7 and Table 1 compare the average
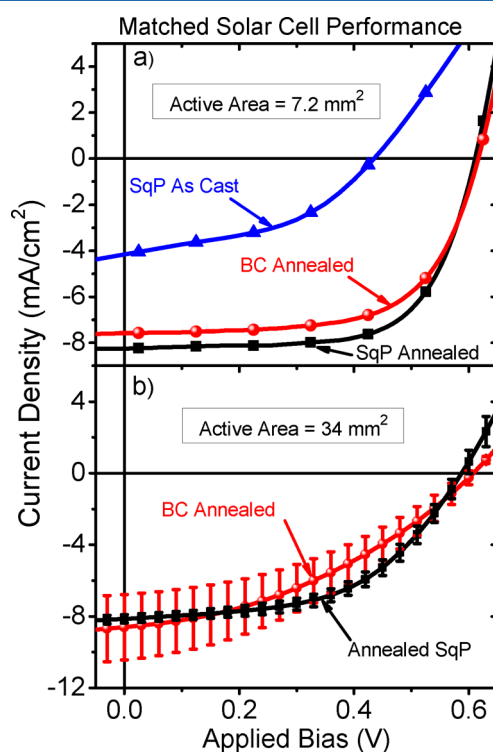

Figure 7. (a) Comparison of SqP vs BC device performance in the standard ITO/PEDOT:PSS/active-layer/Ca/Al device structure. (b) Larger-area device performance of matched SqP and BC solar cells. The enhanced film quality of SqP devices results in better scalability when compared to traditional BC as well as a lower overall device shunt resistance. The error bars in (b) represent one standard deviation obtained from averaging over eight devices; the error bars for (a) are given in Table 1. Other device parameters are summarized in Tables 1 and 2 (see also Figure 8).

photovoltaic performance of matched 1:0.8 mass ratio P3HT:PCBM SqP and BC active layers in standard ITO(150 nm)/PEDOT:PSS(35 nm)/active-layer(165 nm)/Ca(10 nm)/ Al(70 nm) devices under AM1.5 illumination. The data show

Table 1. Photovoltaic Performance of Composition and Thickness Matched SqP and BC Solar Cells[a]

active layer	active area (mm^2)	J_{SC} (mA/cm^2)	V_{OC} (mV)	FF (%)	PCE (%)
annealed SqP	7.2	8.3 ± 0.4	610 ± 8	66 ± 1	3.4 ± 0.2
annealed BC	7.2	7.6 ± 0.5	622 ± 6	61 ± 3	2.9 ± 0.3
as-cast SqP	7.2	4.2 ± 0.3	429 ± 25	44 ± 4	0.8 ± 0.1
annealed SqP	34	8.3 ± 0.5	580 ± 10	52 ± 3	2.5 ± 0.2
annealed BC	34	8.7 ± 1.7	590 ± 10	39 ± 7	2.0 ± 0.4

[a]Each value for 7.2 mm^2 active area devices is averaged over ~30 solar cells made on multiple substrates over multiple device fabrication runs. Each value for 34 mm^2 active area devices was averaged over eight solar cells. Values after the ± represent one standard deviation.

Table 2. Diode Characteristics of Composition and Thickness Matched SqP and BC Solar Cells[a,b]

active layer	n_{id} (dark $J-V$)	n_{id} (V_{OC} vs I)	R_{series} ($\Omega \cdot cm^2$)	R_{shunt} ($\times 10^5$ $\Omega \cdot cm^2$)	av dark carrier density (cm^{-3})	XPS S/C ratio, film/air interface ($\times 10^{-3}$)	XPS S/C ratio, film/glass interface ($\times 10^{-3}$)
annealed BC	1.29 ± 0.04	1.18 ± 0.01	2.4 ± 0.5	3.6 ± 1.7	$<10^{15}$	41 ± 7	12 ± 3
annealed SqP	1.31 ± 0.05	1.19 ± 0.03	2.4 ± 0.4	19.0 ± 13.3	1.1×10^{15}	35 ± 4	17 ± 7
as-cast SqP	1.54 ± 0.12	1.46 ± 0.01	34.9 ± 5.9	1.9 ± 1.2	7.2×10^{15}	1.7 ± 0.3	

[a]The diode characteristics are averaged over ~30 solar cells made on multiple substrates over multiple device fabrication runs. All values after the $\pm$ represent one standard deviation. [b]Device active area of 7.2 mm^2.

that annealed SqP devices are more efficient than the corresponding matched annealed BC devices due to higher short-circuit current densities (J_{SC}) and fill factors (FF). The larger J_{SC} for SqP devices is almost certainly due to stronger P3HT absorption (Figure 4), and the higher fill factor is likely due to a better-ordered network (Figure 5) and higher shunt resistance (Table 2). For completeness, in the Supporting Information (Figure S2) we also compare the performance of SqP and slow-dried BC active-layer devices, which have more crystalline P3HT and thus more similar device efficiencies.

A major reason for the excellent performance of the larger-area SqP active layers in Figure 7b is the overall film quality, which visually is much better than that resulting from traditional BC processing. This observation does not readily manifest itself in the performance of small-area devices (Figure 7a), but does become apparent in larger-area cells (Figure 7b). The error bars in Figure 7b represent one standard deviation for at least eight independent large-area devices. Thus, Figure 7b and Table 1 clearly demonstrate that the SqP fabrication approach is more amenable to scaling than the traditional BC method, as the large-area SqP devices are both more efficient and significantly more reproducible. We are presently working on developing new fullerene casting solvents that will make SqP more conducive to large-area deposition techniques such as printing and blade-coating, which will allow the inherently better SqP film quality and scalable morphology to be fully exploited.

The reason for the differences in film quality between the SqP and BC processing approaches arise from the radically different means by which the donor:acceptor BHJ network is created (Figure 1). Sequential processing is not influenced by film-drying kinetics or cosolubility requirements but instead relies on how well an acceptor molecule (PCBM here) can intercalate into a semicrystalline polymer network. Blend-casting, on the other hand, is more difficult to control because it requires molecularly codissolved solutions that, upon casting, must spontaneously yield the ideal amount of nanoscale phase separation. This type of spontaneous phase-separation process is not well understood and, more importantly, is inherently ultrasensitive to processing conditions (e.g., deposition conditions, film drying kinetics, use of solvent additives, etc.), which is why optimizing the BC film morphology still relies heavily on trial-and-error.[68] Moreover, given the significant differences in BHJ formation, it is reassuring that the SqP method can reproduce and even surpass BC device performance for a set of molecules (i.e., P3HT and PCBM) that are considered to be ideally suited for BC.

Figure 7a and Table 1 also present the photovoltaic performance of matched as-cast SqP devices, which show far inferior performance to annealed versions of both SqP and BC cells.[11] It is well-known that as-cast SqP films have more of a bilayer structure than an intermixed BHJ morphology and that

this structure gives significantly worse photovoltaic performance.[11,17,19] Since comparisons of as-cast and annealed SqP P3HT:PCBM solar cells have been examined in other work,[11,17,19,23,26] we relegate further discussion of as-cast SqP device performance to the Supporting Information.

4.2. Steady-State Device Physics of Matched SqP and BC Films. To further understand how the differences in morphology explored above are manifest in device behavior, we analyzed the open-circuit voltage (V_{OC}) as a function of light intensity (I) (Table 2 and Figure 8a) and the dark diode current density (J) as a function of applied voltage (V) (Table 2 and Figure 8b) for our matched BC and SqP devices. Our methods for obtaining the values in Table 2 are detailed in the Supporting Information. Since one might expect the morphology differences to lead to differences in the recombination process(es) occurring within the device, we focus in this section on the diode ideality factor (n_{id}).[69−73] The ideality factor derives from the slope of the linear region in a semilogarithmic dark $J-V$ or V_{OC} vs I plot and primarily reflects the dominant recombination mechanism occurring within the semiconductor active layer. Ideality factors are unitless and typically range from 1 to 2, though values outside this range are possible.[69,74] An ideality factor of 1 is consistent with more ideal band-to-band recombination processes, whereas an ideality factor of 2 is consistent with trap-assisted recombination through midgap states. The recombination processes that give rise to intermediate ideality factors between 1 and 2 are not readily evident and must be evaluated on a contextual basis, though these values are often closely tied to trap-assisted recombination.[71]

Table 2 shows that the ideality factors we extract for matched-annealed SqP and BC devices are identical whether evaluated from dark $J-V$ curves or from V_{OC} vs I. The reason for the discrepancy between n_{id}'s obtained from dark $J-V$ and from V_{OC} vs I analysis is the subject of some controversy and is discussed in detail elsewhere.[69,75] As mentioned above, the nonunity ideality factors in Table 2 for both the BC and SqP devices are consistent with a significant amount of trap-assisted recombination, likely through a distribution of trap energies.[70−72] If the ideality factor is considered to be representative of bulk recombination processes, then our results surprisingly suggest that the dominant recombination mechanism(s) is(are) the same in matched-annealed SqP and BC films, despite the rather significant differences in overall crystallinity and more subtle differences in BHJ network morphology. Our results thus suggest that the interfacial density of states and recombination processes are similar in optimized SqP and BC films and not as strongly correlated with domain size and molecular ordering as one might have expected. This conclusion is also consistent with our subgap EQE and transient measurements, discussed below.
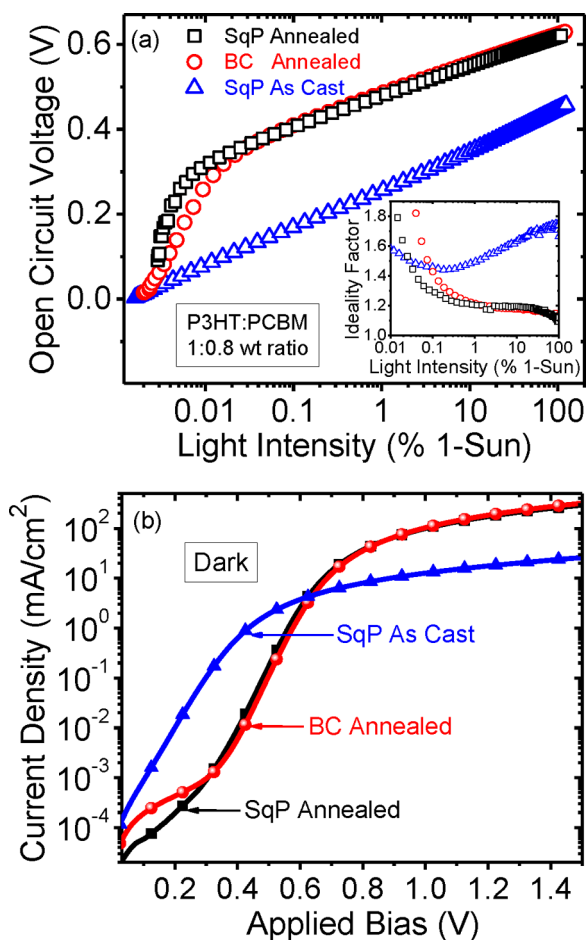
Figure 8. Photovoltaic behavior of matched, annealed BC (red cirlcles/curves), and as-cast (blue triangles/curves) and annealed (black squares/curves) SqP devices. (a) V_{OC} as a function of light intensity. The V_{OC} of annealed SqP devices rises faster at lower light intensity than that of BC devices because of a larger shunt resistance. Beyond the shunt-dominated regime, the annealed SqP V_{OC} almost uniformly tracks the annealed BC except for a ~12 mV offset. The inset shows the differential ideality factor. (b) Dark $J-V$ characteristics of 7.2 mm^2 active area devices. Clearly, the annealed SqP has significantly less leakage current than the annealed BC while the as-cast SqP has both higher series resistance and lower shunt resistance.

Further analysis of the $J-V$ curves in Figure 8 also allows us to extract the effective external series and shunt resistances of our matched BC and SqP devices (see Supporting Information for analysis details). When we perform this analysis, also summarized in Table 2, we find that annealed SqP devices have a substantially higher shunt resistance than the BC devices, which can be readily observed in the low bias region of Figure 8b. This is likely another manifestation of the visually better film quality of annealed SqP devices, since macroscopic film defects facilitate leakage current. The effective series resistances for matched BC and SqP annealed active layers, on the other hand, are identical, which indicates that the devices are well matched in terms of contact and interlayer properties. As-cast SqP dark device data is discussed in the Supporting Information.

4.3. Recombination Kinetics and Interfacial Density of States of Matched SqP and BC OPVs. Given that the $J-V$ curves of matched-annealed SqP and BC devices (over small active areas) are so similar, the question is: do the morphology

differences that result from the different processing routes make any noticeable difference in the device physics that is not evident from the $J-V$ curves? To answer this question, we first used transient photovoltage (TPV) and transient photocurrent (TPC) techniques to study the recombination kinetics in our matched films. TPV measures the return-to-steady-state decay of the V_{OC} after a small light-pulse perturbation, while TPC examines the response of the J_{SC} to this same light pulse. TPV provides a good window into the recombination kinetics since at V_{OC}, the excess perturbation charges must decay via recombination.[76] TPC, on the other hand, is dominated by carrier sweep-out and is therefore used to measure the amount of photogenerated charge caused by the perturbation pulse. TPC and TPV have been widely used in the organic solar cell community to determine excess-carrier recombination rates as a function of total average excess-carrier density (n).[77−83] The information obtained from TPC, TPV, and related techniques are highly relevant because the entire $J-V$ curve at multiple light intensities can be reconstructed from the analysis.[6,80,82,84−86]

Figure 9 compares the average excess-carrier recombination properties of two annealed SqP (black squares) and two
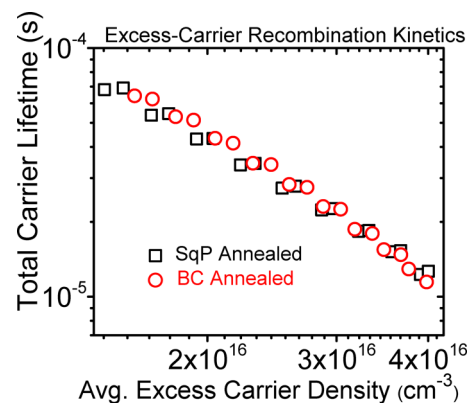

Figure 9. Total carrier lifetime plotted as a function of total (trapped plus free) average excess-carrier concentration relative to short circuit in the dark, as obtained from analysis of TPV and TPC measurements. The data for each active-layer type is composed of the results from two different solar cells. These recombination kinetics suggest that the interfacial electronic properties of matched annealed SqP (black squares) and BC (red circles) films is essentially identical, despite the differences in component crystallinity and BHJ architecture between them.

annealed BC (red circles) devices as derived from our TPC/TPV analysis (see Supporting Information for details). As is typically found in polymer:fullerene BHJs, the carrier lifetime (τ) is observed to depend more strongly on the total average carrier concentration (n) than would be expected for the case of ideal band-to-band recombination ($\tau \sim n^{-1}$). The relationship that we observe ($\tau \sim n^{-\gamma}$, where $\gamma > 1$) is consistent with a significant contribution by trap-assisted (Shockley−Read−Hall)[87] recombination through a distribution of trap energies, which is also in agreement with our ideality factor analysis above.[71−73] Thus, Figure 9 shows that despite the modestly different nanometer-scale morphologies and significantly different molecular ordering, the SqP and BC processing routes yield devices that have essentially identical recombination kinetics as measured by TPC/TPV. This again suggests that although the nanoscale architecture of SqP and BC BHJ films is different, the

recombination kinetics are not terribly sensitive to these structural differences, but instead are likely dominated by interfacial structure and mixing at the boundary of P3HT and PCBM domains.

To further confirm these ideas, we directly measured the interfacial density of states distributions in these BHJ structures using subgap external quantum efficiency (EQE) measurements.[74] Subgap EQE details a solar cell's photoresponse to subenergy-gap photoexcitation and has previously been interpreted as reflecting the joint density of interfacial states in polymer:fullerene BHJs.[88] The lowest energy portion of the EQE spectrum in particular has been shown to correlate well with solar cell performance, dark diode characteristics, and intentionally introduced defects.[70,88−90]

Figure 10 shows the EQE of our matched annealed SqP (black curve/square) and BC (red curve/circles) devices. The
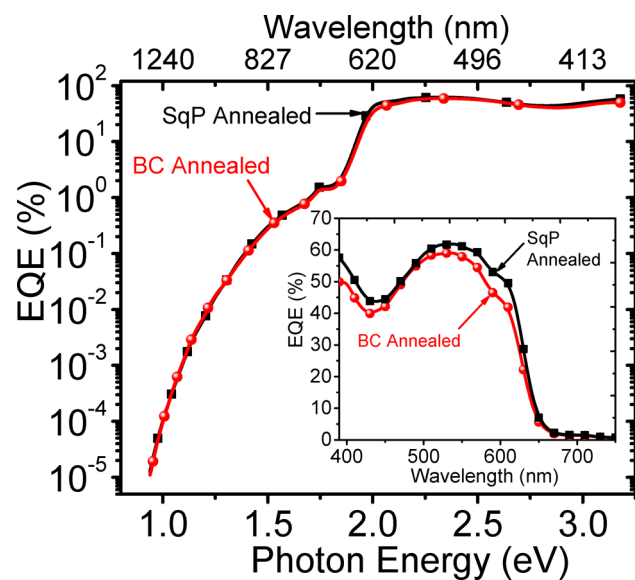

Figure 10. EQE spectra for matched annealed BC (red curves/circles) and SqP (black curves/circles) devices. The linear scale EQE (inset) is consistent with the differences in absorption in Figure 4. The subgap EQE signal involving interfacial transitions (<∼1.5 eV) is essentially identical for annealed SqP and BC devices.

differences in the above-gap EQE (Figure 10 inset) are consistent with the differences in absorption seen above in Figure 4; the higher EQE at ≈600 nm reflects the fact that the P3HT is more crystalline in the SqP case. When integrated against the AM 1.5G solar spectrum, the predicted J_{SC} values are 8.05 and 7.29 mA/cm^2 for the annealed SqP and BC devices, respectively, in reasonable agreement with the measured J_{SC} values in Table 1. Interestingly, the subgap EQE signal involving interfacial transitions (below ≈1.5 eV) is nearly identical for annealed SqPs and BCs, again suggesting that the two routes yield essentially the same interfacial electronic properties despite the measured differences in morphology, molecular crystallinity, and doping. More specifically, these similarities indicate that, in these BHJs, the overall molecular ordering and nanoscale morphology is not necessarily directly coupled to the molecular structure at the heterojunction interfaces. Indeed, the interfacial properties for optimal P3HT:PCBM appear to be highly robust, which is perhaps one reason why this materials combination consistently photogenerates mobile charges with high yield.

Taken together, Table 2 and Figures 7−10 jointly support our broad claim that, despite modestly different nanometer-scale morphologies and doping densities and significant differences in molecular ordering and crystallinity, the interfacial electronic processes in matched annealed SqP and BC photovoltaic devices are essentially identical.

5. CONCLUSIONS

In summary, we have presented an extensive comparison of the morphology and device performance/characteristics of thickness- and composition-matched P3HT:PCBM SqP and BC active layers. Since the composition of SqP active layers was not previously known to an accurate degree, we invented a method for obtaining the overall composition of a polymer/fullerene SqP film based on redissolving and analyzing the dilute-solution absorption spectrum. We showed that our solution-based method is both accurate and reproducible. When applying this technique, we found that the optimal composition of P3HT:PCBM SqP and BC active layers falls in the same range (44−50 mass % PCBM). Despite the similarity in composition, annealed SqP active layers yield better device performance due to both enhanced absorption from more crystalline P3HT and superior film quality. The improved film quality of SqP active layers plays a major role in enhancing the performance of larger-area devices, which indicates that the SqP approach is more amenable to scaling than the traditional BC approach. GIXD, UV−vis absorption, and energy-filtered transmission electron tomography all show that annealed SqP active layers have a finer-scale blend morphology as well as more ordered polymer and fullerene domains when compared to equivalently processed BC active layers. XPS analysis reveals a top interface for SqP films that is slightly richer in PCBM when compared to matched BC active layers, an observation also supported by CELIV measurements of PCBM doping at the cathode interface. Despite these clear morphological differences, measurements of the carrier recombination kinetics from TPC and TPV experiments and the distribution of interface states from subgap EQE measurements all indicate that the interfacial electronic processes occurring at P3HT:PCBM heterojunctions are essentially identical for matched annealed SqP and BC active layers. This suggests that modest differences in network order do not make a large impact on the interfacial electronic processes, perhaps explaining why the BHJ morphology has worked so well despite the lack of processing control over its nanometer-scale architecture.

■ ASSOCIATED CONTENT

ⓢ Supporting Information

BC film absorbance and device performance sensitivity to drying conditions, discussion of as-cast device physics, CELIV traces, detailed experimental procedures, example $J−V$ fits/analysis, and 2-D GIXD intensity plots. This material is available free of charge via the Internet at http://pubs.acs.org.

■ AUTHOR INFORMATION

Corresponding Authors
*E-mail tolbert@chem.ucla.edu; Tel (310) 206-4767 (S.H.T.).
*E-mail schwartz@chem.ucla.edu; Tel (310) 206-4113 (B.J.S.).

Notes

The authors declare no competing financial interest.

■ REFERENCES

(1) Deibel, C.; Dyakonov, V. Polymer-Fullerene Bulk Heterojunction Solar Cells. *Rep. Prog. Phys.* **2010**, *73*, 096401.

(2) He, Z.; Zhong, C.; Su, S.; Xu, M.; Wu, H.; Cao, Y. Enhanced Power-Conversion Efficiency in Polymer Solar Cells Using an Inverted Device Structure. *Nat. Photonics* **2012**, *6*, 591–595.

(3) Li, G.; Zhu, R.; Yang, Y. Polymer Solar Cells. *Nat. Photonics* **2012**, *6*, 153–161.

(4) You, J.; Chen, C.-C.; Hong, Z.; Yoshimura, K.; Ohya, K.; Xu, R.; Ye, S.; Gao, J.; Li, G.; Yang, Y. 10.2% Power Conversion Efficiency Polymer Tandem Solar Cells Consisting of Two Identical Sub-Cells. *Adv. Mater.* **2013**, *25*, 3973–3978.

(5) You, J.; Dou, L.; Yoshimura, K.; Kato, T.; Ohya, K.; Moriarty, T.; Emery, K.; Chen, C.-C.; Gao, J.; Li, G.; et al. A Polymer Tandem Solar Cell with 10.6% Power Conversion Efficiency. *Nat. Commun.* **2013**, *4*, 1446.

(6) Dibb, G. F. A.; Jamieson, F. C.; Maurano, A.; Nelson, J.; Durrant, J. R. Limits on the Fill Factor in Organic Photovoltaics: Distinguishing Nongeminate and Geminate Recombination Mechanisms. *J. Phys. Chem. Lett.* **2013**, *4*, 803–808.

(7) Kirchartz, T.; Agostinelli, T.; Campoy-Quiles, M.; Gong, W.; Nelson, J. Understanding the Thickness-Dependent Performance of Organic Bulk Heterojunction Solar Cells: The Influence of Mobility, Lifetime, and Space Charge. *J. Phys. Chem. Lett.* **2012**, *3*, 3470–3475.

(8) Collins, B. A.; Tumbleston, J. R.; Ade, H. Miscibility, Crystallinity, and Phase Development in P3HT/PCBM Solar Cells: Toward an Enlightened Understanding of Device Morphology and Stability. *J. Phys. Chem. Lett.* **2011**, *2*, 3135–3145.

(9) Brabec, C. J.; Heeney, M.; McCulloch, I.; Nelson, J. Influence of Blend Microstructure on Bulk Heterojunction Organic Photovoltaic Performance. *Chem. Soc. Rev.* **2011**, *40*, 1185–1199.

(10) Schmidt, K.; Tassone, C. J.; Niskala, J. R.; Yiu, A. T.; Lee, O. P.; Weiss, T. M.; Wang, C.; Fréchet, J. M. J.; Beaujuge, P. M.; Toney, M. F. A Mechanistic Understanding of Processing Additive-Induced Efficiency Enhancement in Bulk Heterojunction Organic Solar Cells. *Adv. Mater.* **2014**, *26*, 300–305.

(11) Ayzner, A. L.; Tassone, C. J.; Tolbert, S. H.; Schwartz, B. J. Reappraising the Need for Bulk Heterojunctions in Polymer-Fullerene Photovoltaics: The Role of Carrier Transport in All-Solution-Processed P3HT/PCBM Bilayer Solar Cells. *J. Phys. Chem. C* **2009**, *113*, 20050–20060.

(12) Wang, D. H.; Lee, H. K.; Choi, D.-G.; Park, J. H.; Park, O. O. Solution-Processable Polymer Solar Cells from a Poly(3-Hexylthiophene)/6,6-Phenyl C-61-Butyric Acidmethyl Ester Concentration Graded Bilayers. *Appl. Phys. Lett.* **2009**, *95*, 043505.

(13) Hui, L.; Yong-Fang, L.; Jizheng, W. Optimizing Performance of Layer-by-Layer Processed Polymer Solar Cells. *Appl. Phys. Lett.* **2012**, *101*, 033907.

(14) Kim, D. H.; Mei, J.; Ayzner, A. L.; Schmidt, K.; Giri, G.; Appleton, A. L.; Toney, M. F.; Bao, Z. Sequentially Solution-Processed, Nanostructured Polymer Photovoltaics Using Selective Solvents. *Energy Environ. Sci.* **2014**, *7*, 1103–1109.

(15) Hui, L.; Jizheng, W. Layer-by-Layer Processed High-Performance Polymer Solar Cells. *Appl. Phys. Lett.* **2012**, *101*, 263901.

(16) Oh, J. Y.; Lee, T. I.; Jang, W. S.; Chae, S. S.; Park, J. H.; Lee, H. W.; Myoung, J.-M.; Baik, H. K. Mass Production of a 3D Non-Woven Nanofabric with Crystalline P3HT Nanofibrils for Organic Solar Cells. *Energy Environ. Sci.* **2013**, *6*, 910–917.

(17) Lee, K. H.; Schwenn, P. E.; Smith, A. R. G.; Cavaye, H.; Shaw, P. E.; James, M.; Krueger, K. B.; Gentle, I. R.; Meredith, P.; Burn, P. L. Morphology of All-Solution-Processed "Bilayer" Organic Solar Cells. *Adv. Mater.* **2011**, *23*, 766–770.

(18) Rochester, C. W.; Mauger, S. A.; Moule, A. J. Investigating the Morphology of Polymer/Fullerene Layers Coated Using Orthogonal Solvents. *J. Phys. Chem. C* **2012**, *116*, 7287–7292.

(19) Lee, K. H.; Zhang, Y.; Burn, P. L.; Gentle, I. R.; James, M.; Nelson, A.; Meredith, P. Correlation of Diffusion and Performance in Sequentially Processed P3HT/PCBM Heterojunction Films by Time-Resolved Neutron Reflectometry. *J. Mater. Chem. C* **2013**, *1*, 2593–2598.

(20) Nardes, A. M.; Ayzner, A. L.; Hammond, S. R.; Ferguson, A. J.; Schwartz, B. J.; Kopidakis, N. Photoinduced Charge Carrier Generation and Decay in Sequentially Deposited Polymer/Fullerene Layers: Bulk Heterojunction vs Planar Interface. *J. Phys. Chem. C* **2012**, *116*, 7293–7305.

(21) Chen, D.; Liu, F.; Wang, C.; Nakahara, A.; Russell, T. P. Bulk Heterojunction Photovoltaic Active Layers via Bilayer Interdiffusion. *Nano Lett.* **2011**, *11*, 2071–2078.

(22) Collins, B. A.; Gann, E.; Guignard, L.; He, X.; McNeill, C. R.; Ade, H. Molecular Miscibility of Polymer-Fullerene Blends. *J. Phys. Chem. Lett.* **2010**, *1*, 3160–3166.

(23) Gadisa, A.; Tumbleston, J. R.; Ko, D.-H.; Aryal, M.; Lopez, R.; Samulski, E. T. The Role of Solvent and Morphology on Miscibility of Methanofullerene and Poly(3-Hexylthiophene). *Thin Solid Films* **2012**, *520*, 5466–5471.

(24) Loiudice, A.; Rizzo, A.; Latini, G.; Nobile, C.; de Giorgi, M.; Gigli, G. Graded Vertical Phase Separation of Donor/Acceptor Species for Polymer Solar Cells. *Sol. Energy Mater. Sol. Cells* **2012**, *100*, 147–152.

(25) Treat, N. D.; Brady, M. A.; Smith, G.; Toney, M. F.; Kramer, E. J.; Hawker, C. J.; Chabinyc, M. L. Interdiffusion of PCBM and P3HT Reveals Miscibility in a Photovoltaically Active Blend. *Adv. Energy Mater.* **2011**, *1*, 82–89.

(26) Loiudice, A.; Rizzo, A.; Biasiucci, M.; Gigli, G. Bulk Heterojunction Versus Diffused Bilayer: The Role of Device Geometry in Solution P-Doped Polymer-Based Solar Cells. *J. Phys. Chem. Lett.* **2012**, *3*, 1908–1915.

(27) Vohra, V.; Campoy-Quiles, M.; Garriga, M.; Murata, H. Organic Solar Cells Based on Nanoporous P3HT Obtained from Self-Assembled P3HT:PS Templates. *J. Mater. Chem.* **2012**, *22*, 20017–20025.

(28) Vohra, V.; Higashimine, K.; Murakami, T.; Murata, H. Addition of Regiorandom Poly(3-Hexylthiophene) to Solution Processed Poly(3-Hexylthiophene):[6,6]-Phenyl-C61-Butyric Acid Methyl Ester Graded Bilayers to Tune the Vertical Concentration Gradient. *Appl. Phys. Lett.* **2012**, *101*, 173301.

(29) Vohra, V.; Higashimine, K.; Tsuzaki, S.; Ohdaira, K.; Murata, H. Formation of Vertical Concentration Gradients in Poly(3-Hexylth-

iophene-2,5-Diyl): Phenyl-C61-Butyric Acid Methyl Ester-Graded Bilayer Solar Cells. *Thin Solid Films* **2013**, *554*, 41–45.

(30) Vohra, V.; Arrighetti, G.; Barba, L.; Higashimine, K.; Porzio, W.; Murata, H. Enhanced Vertical Concentration Gradient in Rubbed P3HT:PCBM Graded Bilayer Solar Cells. *J. Phys. Chem. Lett.* **2012**, *3*, 1820–1823.

(31) Li, H.; Qi, Z.; Wang, J. Layer-by-Layer Processed Polymer Solar Cells with Self-Assembled Electron Buffer Layer. *Appl. Phys. Lett.* **2013**, *102*, 213901.

(32) de Villers, B. T.; Tassone, C. J.; Tolbert, S. H.; Schwartz, B. J. Improving the Reproducibility of P3HT:PCBM Solar Cells by Controlling the PCBM/Cathode Interface. *J. Phys. Chem. C* **2009**, *113*, 18978–18982.

(33) Tao, C.; Aljada, M.; Shaw, P. E.; Lee, K. H.; Cavaye, H.; Balfour, M. N.; Borthwick, R. J.; James, M.; Burn, P. L.; Gentle, I. R.; et al. Controlling Hierarchy in Solution-Processed Polymer Solar Cells Based on Crosslinked P3HT. *Adv. Energy Mater.* **2013**, *3*, 105–112.

(34) Liu, B.; Png, R.-Q.; Zhao, L.-H.; Chua, L.-L.; Friend, R. H.; Ho, P. K. H. High Internal Quantum Efficiency in Fullerene Solar Cells Based on Crosslinked Polymer Donor Networks. *Nat. Commun.* **2012**, *3*, 1321.

(35) Park, H. J.; Lee, J. Y.; Lee, T.; Guo, L. J. Advanced Heterojunction Structure of Polymer Photovoltaic Cell Generating High Photocurrent with Internal Quantum Efficiency Approaching 100%. *Adv. Energy Mater.* **2013**, *3*, 1135–1142.

(36) Yang, H. Y.; Kang, N. S.; Hong, J.-M.; Song, Y.-W.; Kim, T. W.; Lim, J. A. Efficient Bilayer Heterojunction Polymer Solar Cells with Bumpy Donor-Acceptor Interface Formed by Facile Polymer Blend. *Org. Electron.* **2012**, *13*, 2688–2695.

(37) Zhu, R.; Kumar, A.; Yang, Y. Polarizing Organic Photovoltaics. *Adv. Mater.* **2011**, *23*, 4193–4198.

(38) Kim, T.; Yang, S. J.; Kim, S. K.; Choi, H. S.; Park, C. R. Preparation of PCDTBT Nanofibers with a Diameter of 20 nm and Their Application to Air-Processed Organic Solar Cells. *Nanoscale* **2014**, *6*, 2847–2854.

(39) Oh, J. Y.; Lee, T. I.; Jang, W. S.; Chae, S. S.; Park, J. H.; Lee, H. W.; Myoung, J.-M.; Baik, H. K. Mass Production of a 3d Non-Woven Nanofabric with Crystalline P3HT Nanofibrils for Organic Solar Cells. *Energy Environ. Sci.* **2013**, *6*, 910–917.

(40) Han, X.; Wu, Z.; Sun, B. Enhanced Performance of Inverted Organic Solar Cell by a Solution-Based Fluorinated Acceptor Doped P3HT:PCBM Layer. *Org. Electron.* **2013**, *14*, 1116–1121.

(41) Cheng, P.; Hou, J.; Li, Y.; Zhan, X. Layer-by-Layer Solution-Processed Low-Bandgap Polymer-PC$_{61}$BM Solar Cells with High Efficiency. *Adv. Energy Mater.* **2014**, DOI: 10.1002/aenm.201301349.

(42) Yang, B.; Yuan, Y.; Huang, J. Reduced Bimolecular Charge Recombination Loss in Thermally Annealed Bilayer Heterojunction Photovoltaic Devices with Large External Quantum Efficiency and Fill Factor. *J. Phys. Chem. C* **2014**, *118*, 5196–5202.

(43) Ayzner, A. L.; Doan, S. C.; de Villers, B. T.; Schwartz, B. J. Ultrafast Studies of Exciton Migration and Polaron Formation in Sequentially Solution-Processed Conjugated Polymer/Fullerene Quasi-Bilayer Photovoltaics. *J. Phys. Chem. Lett.* **2012**, *3*, 2281–2287.

(44) Dang, M. T.; Hirsch, L.; Wantz, G. P3HT:PCBM, Best Seller in Polymer Photovoltaic Research. *Adv. Mater.* **2011**, *23*, 3597–3602.

(45) Wang, D. H.; Moon, J. S.; Seifter, J.; Jo, J.; Park, J. H.; Park, O. O.; Heeger, A. J. Sequential Processing: Control of Nanomorphology in Bulk Heterojunction Solar Cells. *Nano Lett.* **2011**, *11*, 3163–3168.

(46) Moon, J. S.; Takacs, C. J.; Sun, Y.; Heeger, A. J. Spontaneous Formation of Bulk Heterojunction Nanostructures: Multiple Routes to Equivalent Morphologies. *Nano Lett.* **2011**, *11*, 1036–1039.

(47) Dang, M. T.; Hirsch, L.; Wantz, G.; Wuest, J. D. Controlling the Morphology and Performance of Bulk Heterojunctions in Solar Cells. Lessons Learned from the Benchmark Poly(3-Hexylthiophene):[6,6]-Phenyl-C61-Butyric Acid Methyl Ester System. *Chem. Rev.* **2013**, *113*, 3734–3765.

(48) Müller, C.; Ferenczi, T. A. M.; Campoy-Quiles, M.; Frost, J. M.; Bradley, D. D. C.; Smith, P.; Stingelin-Stutzmann, N.; Nelson, J.

(49) Clark, J.; Silva, C.; Friend, R. H.; Spano, F. C. Role of Intermolecular Coupling in the Photophysics of Disordered Organic Semiconductors: Aggregate Emission in Regioregular Polythiophene. *Phys. Rev. Lett.* **2007**, *98*, 206406.

Binary Organic Photovoltaic Blends: A Simple Rationale for Optimum Compositions. *Adv. Mater.* **2008**, *20*, 3510–3515.

(50) Li, G.; Shrotriya, V.; Huang, J. S.; Yao, Y.; Moriarty, T.; Emery, K.; Yang, Y. High-Efficiency Solution Processable Polymer Photovoltaic Cells by Self-Organization of Polymer Blends. *Nat. Mater.* **2005**, *4*, 864–868.

(51) Lin, Y.; Ma, L.; Li, Y.; Liu, Y.; Zhu, D.; Zhan, X. Small-Molecule Solar Cells with Fill Factors up to 0.75 via a Layer-by-Layer Solution Process. *Adv. Energy Mater.* **2013**, *4*, 1300626.

(52) Moule, A. J.; Meerholz, K. Interference Method for the Determination of the Complex Refractive Index of Thin Polymer Layers. *Appl. Phys. Lett.* **2007**, *91*, 061901.

(53) Ma, W. L.; Yang, C. Y.; Gong, X.; Lee, K.; Heeger, A. J. Thermally Stable, Efficient Polymer Solar Cells with Nanoscale Control of the Interpenetrating Network Morphology. *Adv. Funct. Mater.* **2005**, *15*, 1617–1622.

(54) Herzing, A. a.; Richter, L. J.; Anderson, I. M. 3D Nanoscale Characterization of Thin-Film Organic Photovoltaic Device Structures via Spectroscopic Contrast in the TEM 1. *J. Phys. Chem. C* **2010**, *114*, 17501–17508.

(55) Drummy, L. F.; Davis, R. J.; Moore, D. L.; Durstock, M.; Vaia, R. A.; Hsu, J. W. P. Molecular-Scale and Nanoscale Morphology of P3HT:PCBM Bulk Heterojunctions: Energy-Filtered TEM and Low-Dose HREM. *Chem. Mater.* **2011**, *23*, 907–912.

(56) Pfannmöller, M.; Flügge, H.; Benner, G.; Wacker, I.; Sommer, C.; Hanselmann, M.; Schmale, S.; Schmidt, H.; Hamprecht, F. A.; Rabe, T.; et al. Visualizing a Homogeneous Blend in Bulk Heterojunction Polymer Solar Cells by Analytical Electron Microscopy. *Nano Lett.* **2011**, *11*, 3099–3107.

(57) Herzing, A. A.; Ro, H.-W.; Soles, C. L.; DeLongchamp, D. M. Visualization of Phase Evolution in Model Organic Photovoltaic Structures Electron Microscopy. *ACS Nano* **2013**, *7*, 7937–7944.

(58) Gevaerts, V. S.; Koster, L. J. A.; Wienk, M. M.; Janssen, R. A. J. Discriminating between Bilayer and Bulk Heterojunction Polymer: Fullerene Solar Cells Using the External Quantum Efficiency. *ACS Appl. Mater. Interfaces* **2011**, *3*, 3252–3255.

(59) Campoy-Quiles, M.; Ferenczi, T.; Agostinelli, T.; Etchegoin, P. G.; Kim, Y.; Anthopoulos, T. D.; Stavrinou, P. N.; Bradley, D. D. C.; Nelson, J. Morphology Evolution via Self-Organization and Lateral and Vertical Diffusion in Polymer:Fullerene Solar Cell Blends. *Nat. Mater.* **2008**, *7*, 158–164.

(60) Vaynzof, Y. V. Y.; Kabra, D.; Zhao, L. H.; Chua, L. L.; Steiner, U.; Friend, R. H. Surface-Directed Spinodal Decomposition in Poly 3-hexylthiophene and C(61)-Butyric Acid Methyl Ester Blends. *ACS Nano* **2010**, *5*, 329–336.

(61) Ratcliff, E. L.; Jenkins, J. L.; Nebesny, K.; Armstrong, N. R. Electrodeposited, "Textured" Poly(3-Hexyl-Thiophene) (E-P3HT) Films for Photovoltaic Applications. *Chem. Mater.* **2008**, *20*, 5796–5806.

(62) Xu, Z.; Chen, L.-M.; Yang, G.; Huang, C.-H.; Hou, J.; Wu, Y.; Li, G.; Hsu, C.-S.; Yang, Y. Vertical Phase Separation in Poly(3-Hexylthiophene): Fullerene Derivative Blends and Its Advantage for Inverted Structure Solar Cells. *Adv. Funct. Mater.* **2009**, *19*, 1227–1234.

(63) Orimo, A.; Masuda, K.; Honda, S.; Benten, H.; Ito, S.; Ohkita, H.; Tsuji, H. Surface Segregation at the Aluminum Interface of Poly(3-Hexylthiophene)/Fullerene Solar Cells. *Appl. Phys. Lett.* **2010**, *96*, 043305.

(64) Juska, G.; Arlauskas, K.; Viliunas, M.; Kocka, J. Extraction Current Transients: New Method of Study of Charge Transport in Microcrystalline Silicon. *Phys. Rev. Lett.* **2000**, *84*, 4946–4949.

(65) Mauger, S. A.; Chang, L.; Friedrich, S.; Rochester, C. W.; Huang, D. M.; Wang, P.; Moulé, A. J. Self-Assembly of Selective Interfaces in Organic Photovoltaics. *Adv. Funct. Mater.* **2013**, *23*, 1935–1946.

(66) Parnell, A. J.; Dunbar, A. D. F.; Pearson, A. J.; Staniec, P. A.; Dennison, A. J. C.; Hamamatsu, H.; Skoda, M. W. A.; Lidzey, D. G.; Jones, R. A. L. Depletion of PCBM at the Cathode Interface in P3HT/PCBM Thin Films as Quantified via Neutron Reflectivity Measurements. *Adv. Mater.* **2010**, *22*, 2444−2447.

(67) Kirchartz, T.; Gong, W.; Hawks, S. A.; Agostinelli, T.; MacKenzie, R. C. I.; Yang, Y.; Nelson, J. Sensitivity of the Mott-Schottky Analysis in Organic Solar Cells. *J. Phys. Chem. C* **2012**, *116*, 7672−7680.

(68) Heeger, A. J. 25th Anniversary Article: Bulk Heterojunction Solar Cells: Understanding the Mechanism of Operation. *Adv. Mater.* **2014**, *26*, 10−28.

(69) Kirchartz, T.; Deledalle, F.; Tuladhar, P. S.; Durrant, J. R.; Nelson, J. On the Differences between Dark and Light Ideality Factor in Polymer:Fullerene Solar Cells. *J. Phys. Chem. Lett.* **2013**, *4*, 2371−2376.

(70) Street, R. A.; Schoendorf, M. Interface State Recombination in Organic Solar Cells. *Phys. Rev. B* **2010**, *81*, 205307.

(71) Kirchartz, T.; Pieters, B. E.; Kirkpatrick, J.; Rau, U.; Nelson, J. Recombination via Tail States in Polythiophene:Fullerene Solar Cells. *Phys. Rev. B* **2011**, *83*, 115209.

(72) Foertig, A.; Rauh, J.; Dyakonov, V.; Deibel, C. Shockley Equation Parameters of P3HT:PCBM Solar Cells Determined by Transient Techniques. *Phys. Rev. B* **2012**, *86*, 115302.

(73) Credgington, D.; Durrant, J. R. Insights from Transient Optoelectronic Analyses on the Open-Circuit Voltage of Organic Solar Cells. *J. Phys. Chem. Lett.* **2012**, *3*, 1465−1478.

(74) Street, R. A.; Krakaris, A.; Cowan, S. R. Recombination through Different Types of Localized States in Organic Solar Cells. *Adv. Funct. Mater.* **2012**, *22*, 4608−4619.

(75) Wetzelaer, G. A. H.; Kuik, M.; Lenes, M.; Blom, P. W. M. Origin of the Dark-Current Ideality Factor in Polymer:Fullerene Bulk Heterojunction Solar Cells. *Appl. Phys. Lett.* **2011**, *99*, 153506.

(76) Deledalle, F.; Shakya Tuladhar, P.; Nelson, J.; Durrant, J. R.; Kirchartz, T. Understanding the Apparent Charge Density Dependence of Mobility and Lifetime in Organic Bulk Heterojunction Solar Cells. *J. Phys. Chem. C* **2014**, *118*, 8837−8842.

(77) Shuttle, C. G.; O'Regan, B.; Ballantyne, A. M.; Nelson, J.; Bradley, D. D. C.; Durrant, J. R. Bimolecular Recombination Losses in Polythiophene:Fullerene Solar Cells. *Phys. Rev. B* **2008**, *78*, 113201.

(78) Shuttle, C. G.; O'Regan, B.; Ballantyne, A. M.; Nelson, J.; Bradley, D. D. C.; de Mello, J.; Durrant, J. R. Experimental Determination of the Rate Law for Charge Carrier Decay in a Polythiophene: Fullerene Solar Cell. *Appl. Phys. Lett.* **2008**, *92*, 093311.

(79) Shuttle, C. G.; Maurano, A.; Hamilton, R.; O'Regan, B.; de Mello, J. C.; Durrant, J. R. Charge Extraction Analysis of Charge Carrier Densities in a Polythiophene/Fullerene Solar Cell: Analysis of the Origin of the Device Dark Current. *Appl. Phys. Lett.* **2008**, *93*, 183501.

(80) Shuttle, C. G.; Hamilton, R.; O'Regan, B. C.; Nelson, J.; Durrant, J. R. Charge-Density-Based Analysis of the Current-Voltage Response of Polythiophene/Fullerene Photovoltaic Devices. *Proc. Natl. Acad. Sci. U. S. A.* **2010**, *107*, 16448−16452.

(81) Hamilton, R.; Shuttle, C. G.; O'Regan, B.; Hammant, T. C.; Nelson, J.; Durrant, J. R. Recombination in Annealed and Non-annealed Polythiophene/Fullerene Solar Cells: Transient Photovoltage Studies Versus Numerical Modeling. *J. Phys. Chem. Lett.* **2010**, *1*, 1432−1436.

(82) Hawks, S. A.; Deledalle, F.; Yao, J.; Rebois, D. G.; Li, G.; Nelson, J.; Yang, Y.; Kirchartz, T.; Durrant, J. R. Relating Recombination, Density of States, and Device Performance in an Efficient Polymer:Fullerene Organic Solar Cell Blend. *Adv. Energy Mater.* **2013**, *3*, 1201−1209.

(83) Maurano, A.; Hamilton, R.; Shuttle, C. G.; Ballantyne, A. M.; Nelson, J.; O'Regan, B.; Zhang, W. M.; McCulloch, I.; Azimi, H.; Morana, M.; et al. Recombination Dynamics as a Key Determinant of Open Circuit Voltage in Organic Bulk Heterojunction Solar Cells: A Comparison of Four Different Donor Polymers. *Adv. Mater.* **2010**, *22*, 4987−4992.

(84) Dibb, G. F. A.; Kirchartz, T.; Credgington, D.; Durrant, J. R.; Nelson, J. Analysis of the Relationship between Linearity of Corrected Photocurrent and the Order of Recombination in Organic Solar Cells. *J. Phys. Chem. Lett.* **2011**, *2*, 2407−2411.

(85) Maurano, A.; Shuttle, C. G.; Hamilton, R.; Ballantyne, A. M.; Nelson, J.; Zhang, W.; Heeney, M.; Durrant, J. R. Transient Optoelectronic Analysis of Charge Carrier Losses in a Selenophene/Fullerene Blend Solar Cell. *J. Phys. Chem. C* **2011**, *115*, 5947−5957.

(86) Credgington, D.; Jamieson, F. C.; Walker, B.; Nguyen, T.-Q.; Durrant, J. R. Quantification of Geminate and Non-Geminate Recombination Losses within a Solution-Processed Small-Molecule Bulk Heterojunction Solar Cell. *Adv. Mater.* **2012**, *24*, 2135−2141.

(87) Shockley, W.; Read, W. T. Statistics of the Recombinations of Holes and Electrons. *Phys. Rev.* **1952**, *87*, 835−842.

(88) Street, R. A.; Song, K. W.; Northrup, J. E.; Cowan, S. Photoconductivity Measurements of the Electronic Structure of Organic Solar Cells. *Phys. Rev. B* **2011**, *83*, 165207.

(89) Street, R. A.; Davies, D.; Khlyabich, P. P.; Burkhart, B.; Thompson, B. C. Origin of the Tunable Open-Circuit Voltage in Ternary Blend Bulk Heterojunction Organic Solar Cells. *J. Am. Chem. Soc.* **2013**, *135*, 986−989.

(90) Goris, L.; Poruba, A.; Hod'ákova, L.; Vaněček, M.; Haenen, K.; Nesládek, M.; Wagner, P.; Vanderzande, D.; De Schepper, L.; Manca, J. V. Observation of the Subgap Optical Absorption in Polymer-Fullerene Blend Solar Cells. *Appl. Phys. Lett.* **2006**, *88*, 052113.